PSFC/JA-05-7

Observation and Modeling of Ion Cyclotron Range of Frequencies Waves in the Mode Conversion Region of Alcator C-Mod

Y. Lin, S. Wukitch, A. Parisot, J. C. Wright, N. Basse,
P. Bonoli, E. Edlund, L. Lin, and M. Porkolab, G. Schilling*, P. Phillips**

*Princeton Plasma Physics Laboratory, Princeton, NJ 08543, USA
**Fusion Research Center, University of Texas, Austin, TX 78712, USA

February 2005

Plasma Science and Fusion Center
Massachusetts Institute of Technology
Cambridge MA 02139 USA

This work was supported by the U.S. Department of Energy, Grant No. DE-FC02-99ER54512. Reproduction, translation, publication, use and disposal, in whole or in part, by or for the United States government is permitted.

Submitted for publication to *Plasma Physics and Controlled Fusion*

Observation and Modeling of Ion Cyclotron Range of Frequencies Waves in the Mode Conversion Region of Alcator C-Mod

Y. Lin,* S. Wukitch, A. Parisot, J. C. Wright, N. Basse,

P. Bonoli, E. Edlund, L. Lin, and M. Porkolab

Massachusetts Institute of Technology,

Plasma Science and Fusion Center, Cambridge, MA 02139, USA

G. Schilling

Princeton Plasma Physics Laboratory, Princeton, NJ 08543, USA

P. Phillips

Fusion Research Center, University of Texas, Austin, TX 78712, USA

(Dated: February 16, 2005)

Abstract

The fast magnetosonic wave (FW), mode converted ion cyclotron wave (MC ICW) and ion Bernstein wave (MC IBW) have all been observed and unambiguously identified in the mode conversion region of Alcator C-Mod. The influences of the species mix, mode conversion location and $B_{\rm pol}/B_{\rm tot}$ have been studied in D(^{3}He) plasmas at $\rm B_0 \sim 5.4$ T ($f_{\rm RF} = 50$ MHz) and $\rm B_0 \sim 8$ T ($f_{\rm RF} = 78$ MHz). The RF waves were measured by a phase contrast imaging (PCI) system. The experimental observation is compared with the result from a synthetic PCI diagnostic based upon the full wave code TORIC. Good agreement between the observation and modeling has been obtained on the spatial structure of the RF waves. When the mode conversion layer was off axis, both MC ICW and MC IBW were observed. In 5.4 T near axis mode conversion discharges, double hump spatial structure of the MC waves was observed experimentally and reproduced by the synthetic PCI. Such structure is an indication of the up-down asymmetry of the MC ICW. In 8 T near axis mode conversion discharges, we had the first definitive observation of IBW dominated MC in Alcator C-Mod.

*Email: ylin@psfc.mit.edu

I. INTRODUCTION

Ion cyclotron range of frequencies (ICRF) radio wave heating is one of the major auxiliary heating methods in magnetically confined fusion research. An ICRF heated plasma is usually a multi-species plasma, for example, a D(^{3}He) plasma, with ^{3}He as the minority species and deuterium as the majority species. At low ^{3}He concentration ($n_{^3\mathrm{He}}/n_\mathrm{e} \leq 0.05$), the fast magnetosonic wave (fast wave, or FW), launched by the antenna is mostly absorbed by the ^{3}He ions at the ^{3}He cyclotron resonance layer [1]. When the ^{3}He level is moderate ($n_{^3\mathrm{He}}/n_\mathrm{e} \geq 0.1$), the fast wave is partially mode converted to short wavelength waves near the D-^{3}He hybrid layer [2–6]. The mode converted waves may be used to directly heat electrons (for examples, see Refs. [7–11]), drive current [12, 13] and plasma flow [4, 14], etc. In this paper, we report the first comprehensive study on the experimental observation and numerical modeling of ICRF waves, including the fast wave and short wavelength waves, in the mode conversion region of the Alcator C-Mod tokamak.

The ion-ion hybrid layer (MC layer) is defined in the cold plasma limit as $n_\parallel^2 = S$, where $n_\parallel$ is the fast wave refractive index parallel to the B field. $S = 1 - \sum_{j=i,e} \frac{\omega_{\mathrm{pj}}^2}{\omega^2 - \omega_{\mathrm{cj}}^2}$ in the cold plasma approximation, where j denotes particle species, ω_{pj} is the plasma frequency, ω_{cj} is the ion (electron) cyclotron frequency, and ω is the launched RF wave frequency [15]. On the high field side (HFS) of the MC layer, the fast wave can be mode converted to an ion Bernstein wave (IBW), which propagates to the HFS. The MC IBW is a warm plasma slow wave, which only exists with finite ion temperature, with wavelength in the order of $k_\perp \rho_\mathrm{i} \sim 1$, where ρ_i is the Larmor radius and $k_\perp$ is the wave number perpendicular to the magnetic field. It is also a backward wave, i.e., its phase velocity is toward the low field side (LFS). On the LFS of the MC layer, the fast wave can be converted to the MC ion cyclotron wave (ICW), propagating to the LFS. The ICW is a short wavelength wave originating from the magnetic field line rotational transformation in a toroidal plasma confinement device. While the toroidal mode number n_ϕ of the fast wave is fixed by the toroidal symmetry, $n_\parallel$ can be up-shifted to such a level that a short wavelength mode admissible by the local dispersion relation exists in the vicinity of the LFS side of the MC layer [2]. Depending on plasma conditions, such as B field, species concentration, plasma current, density and temperature profile, the relative levels of the fast wave, MC IBW, and MC ICW can vary significantly. In cases where the ratio of poloidal B field strength to total B field strength $B_\mathrm{pol}/B_\mathrm{tot} \ll 1$ near

the MC layer, the MC IBW can be the only MC wave. In a previous experimental study, the MC ICW was observed using a phase contrast imaging (PCI) system in D(H, ^{3}He) plasmas near the H-^{3}He hybrid layer in Alcator C-Mod [3]. In the experiments reported in Ref. [3], the PCI view was on the LFS of the MC layer. The observed wave was identified as the MC ICW by comparing the observations to simulations using a full wave toroidal IC wave code TORIC [16, 17]. Further studies have been performed on mode conversion electron heating and power partition between the MC ICW and IBW [5, 7]. Recent comparison of PCI measurements and TORIC have shown that the TORIC physics kernel and computational algorithm are describing the MC physics well [13, 18]. In the study presented in this paper, the FW, MC ICW and MC IBW have all been observed, sometimes simultaneously, using an upgraded PCI system in D(^{3}He) plasmas. A significantly enhanced TORIC code has also made feasible more realistic comparison between experiments and simulations [6]. Using the upgraded PCI and TORIC, we have studied the influences on the mode conversion of the species mix, MC layer location, and $B_{\rm pol}/B_{\rm tot}$.

The paper is organized as following. Section II describes the experimental setup, the PCI diagnostic, and the synthetic PCI based upon TORIC. In Sec. III, the experimental PCI results are compared with the synthetic PCI results. Off axis mode conversion and near axis mode conversion are presented separately in Sec. III A and III B, followed by Discussion and future work in Sec. IV, and Sec. V gives Summary.

II. SETUP OF EXPERIMENTS AND SIMULATIONS

A. Experimental setup

Alcator C-Mod is a compact ($R \simeq 0.67$ m, $a \simeq 0.22$ m), high field ($B \leq 8.1$ T) tokamak [19]. For experiments reported here, the RF power was provided by a phase-variable 4-strap antenna in J-port (J-antenna) [20]. The RF power level was $P_{\rm RF} \leq 3$ MW. The RF frequency was at 50 MHz for experiments of $B \sim 5.2-5.6$ T and at 78 MHz for experiments of $B \sim 7.7-8.1$ T. The four antenna straps were configured to $[0, \pi, \pi, 0]$ phasing, which gave the peak toroidal mode number of the launched fast wave $n_\phi \simeq \pm 6$ and ± 7. The plasmas were in the low confinement mode (L-mode), comprised of D (majority), ^{3}He (minority), and residual H. The ratio $n_{\rm H}/n_{\rm D}$ was calculated from the spectroscopic measurement of D_α

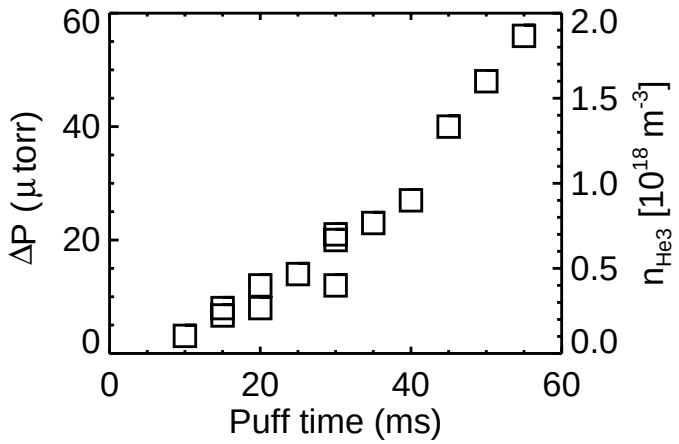

FIG. 1: Gas pressure rise vs. ^{3}He puffing. The left scale is the measured pressure, while the right scale is the equivalent ^{3}He atom density. Data was collected during beam-into-gas calibration for the motional Stark effect (MSE) diagnostic.

and H_α lines at the plasma edge [21]. A flat H/D ratio profile is assumed. ^{3}He was introduced by gas puff in the early stage of the plasma discharge. No diagnostic was available to measure the absolute ^{3}He level. The amount of ^{3}He gas puffed into the vessel is roughly linear as a function of the puffing time (Fig. 1). The ^{3}He level in the plasma is estimated from the mode conversion electron heating (MCEH) profile, which is calculated from the break-in-slope analysis of T_e signals measured by a high spatial and temporal resolution electron cyclotron emission (ECE) system [22]. The power deposition profile is calculated using the following equation,

$$S_{\rm exp}^{\rm mc} \simeq \frac{3}{2} n_{\rm e} \left| \Delta \frac{dT_{\rm e}}{dt} \right|, \tag{1}$$

where $\Delta \frac{dT_e}{dt}$ is the change of the slope of T_e signal before and after a RF shut-off. Since the mode conversion region is narrow, the ^{3}He level can be rather accurately estimated by matching the MCEH profile from TORIC with the one from break-in-slope analysis (see Sec. III A).

B. Phase contrast imaging system and data analysis

The PCI system in Alcator C-Mod measures the line-integrated density fluctuations [23–25]. The PCI laser is located at the E-port and toroidally 216° away from the J-antenna (Fig. 2-(a)). The system presently has 32 channels (vertical chords) covering a window

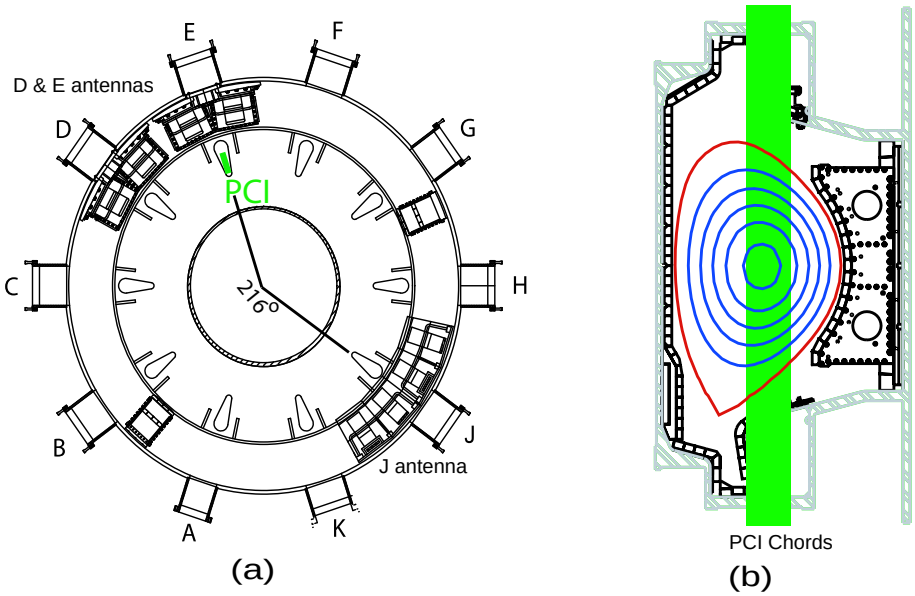

FIG. 2: (a) The toroidal view of Alcator C-Mod. (b) PCI layout.

from major radius $R = 0.64$ to 0.76 m (Fig. 2-(b)). The separation between channels is $\Delta R \simeq 0.4$ cm. As a result, the PCI system can measure wave numbers k_R in the range of $\pm(0.5{-}8)$ cm^{-1} without spatial aliasing. The upper limit of PCI sensitivity is $k_{\rm lim} \simeq 17$ cm^{-1}, determined by the element size of the detectors and optical expansion. To measure waves at the RF frequency, the PCI laser is modulated using two acoustic-optical modulators (AOMs) so that the ICRF waves appear in the PCI signal at the beat-wave frequency. The modulation frequencies are different at different RF frequencies so that the beat-wave frequency is within the digitizer sampling frequency range. The PCI system is most sensitive to waves having vertical wave fronts and propagating in the direction of major radius. Because no vertical resolution is available in the present PCI system, the resulting measurement is a superposition of waves along vertical lines.

The PCI signal in each channel is sampled at 10 MHz for about 0.5 second. Each signal is divided into 10 ms time windows, and the data in each time window are Fourier transformed to the complex spectrum of $A\exp(-i\omega t + i\theta)$. Figure 3 shows an example of the Fourier transformed PCI signal. The coherent peak at $f = \omega_{\rm beat}/2\pi = 970.4$ kHz in this figure is the magnitude of the density fluctuations directly induced by the RF waves. By doing the same analysis on all 32 channels, we can show the spatial structure of the RF waves by the

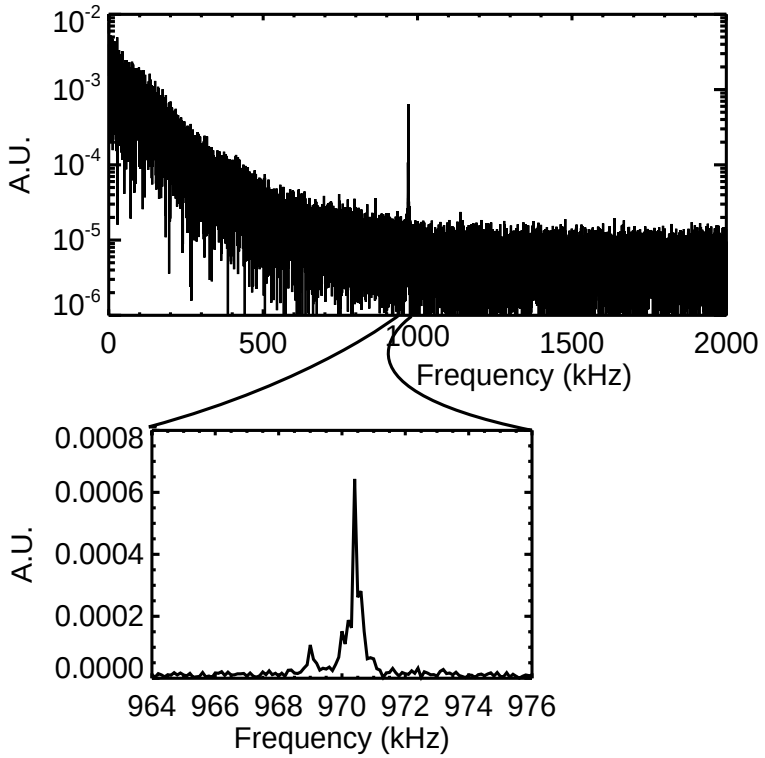

FIG. 3: An example of the Fourier transformed PCI signal. The frequency at the coherent peak, 970.4 kHz, is the beat frequency corresponding to the RF frequency at 50 MHz. The small peak at 969 kHz is a pick-up spurious signal from the detector circuitry.

real and imaginary parts of the complex spectrum at this beat frequency vs. PCI channel locations. From the phase difference $\Delta\theta$ between channels at this beat frequency, we can also calculate a local wave number, $k_{\rm loc} = \Delta\theta/\Delta R$. $k_{\rm loc}$ can approximately represent the dispersion curve of the dominant wave in the PCI view in cases that the wave has nearly vertical wave fronts. Doing Fourier transformation of the complex signal again over all 32 channels, we can calculate the $k_{\rm R}$ spectrum of the PCI measurement. Caution must be taken, however, in interpreting this $k_{\rm R}$ spectrum because mode conversion is substantially localized and a rapid change of wave number often occurs in a narrow region.

The PCI system is calibrated one second before each discharge using a sound burst across the laser beam before the laser beam enters the vacuum window [23]. This calibration provides the information of the width in major radius covered by the PCI view, and also the fluctuation level corresponding to the sound wave. However, it appears inadequate using the sound burst (spherical wave approximation) calibration data to obtain the density

fluctuations for the heterodyne measurement. Using the calibration data above produces density fluctuation levels that are systematically about two orders of magnitude smaller than those estimated from the RF power. The reason may lie in two factors: First, the heterodyne signal is at a much higher frequency (970 kHz for $f_{\rm RF} = 50$ MHz and 1740 kHz for $f_{\rm RF} = 78$ MHz) than the sound wave (15 kHz); Secondly, the conversion efficiencies of the AOMs are not known precisely. In this paper, the PCI results are multiplied by a correction factor of 300 for the 50 MHz experiments, and a factor of 100 for the 78 MHz experiments. The different correction factors may be due to different AOM modulation frequencies and different beat frequencies. After this correction, the experimental result in terms of line-integrated density level is comparable to that from a synthetic PCI (see below). The absolute level calibration for the heterodyne scheme will be the subject of future work.

C. TORIC and synthetic PCI

TORIC is a 2-dimensional (2-D) finite Larmor radius (FLR) full wave RF code [16][17], which solves Maxwell's equations in a toroidal plasma at a fixed RF frequency and a given toroidal number n_ϕ. The electric field is solved in a mixed spectral and finite-element basis. To properly calculate the electron Landau damping (ELD) of the short wavelength modes (IBW/ICW), an imaginary part is added on the FLR coefficient [6][10]. This imaginary part is calculated from the local dispersion relation retaining all orders of $k_\perp \rho_{\rm i}$. This approach calculates the ELD predicted by the local dispersion relation without altering the structure of the equations, or changing the mode conversion efficiency. Additionally, this approach lends itself to efficient numerical calculation resulting from the sparse, block tridiagonal nature of its stiffness matrix. TORIC has been benchmarked with other ICRF codes. It is found to have good agreement with METS [26] in the power absorption on electrons and ions [10]. A qualitative agreement with AORSA2D [4] in the 2-D electric fields in mode conversion scenarios where $k_\perp \rho_{\rm i} \leq 1$ [6] has also been obtained. The code has been extensively benchmarked with ICRF mode conversion experiments in Alcator C-Mod (e.g., see Refs. [5, 7, 13, 18]). The TORIC code in this paper is a parallel version run on a 48-CPU cluster at the MIT Plasma Science and Fusion Center [6]. We use magnetic equilibria reconstructed from EFIT [27] and analytical approximations of the density and temperature profiles in these TORIC runs.

In order to compare the PCI measured density fluctuations at the beat frequency and the RF wave field in the plasma, we have developed a synthetic PCI using TORIC outputs. TORIC calculates the electric field, power deposition profile (such as the mode conversion power deposition profile $S^{\rm mc}_{\rm toric}(n_\phi, \rho)$, where $\rho = r/a$) and the coupling resistance $R_{\rm L}(n_\phi)$ for a one Ampere excitation on the antenna straps. For each plasma discharge of interest, TORIC simulations for toroidal numbers $-20 \le n_\phi \le +20$ are performed. The antenna spectrum beyond $-20 \le n_\phi \le +20$ is negligible. The 2-D density fluctuation $n_{\rm e1}(n_\phi)$ is calculated from the electric field for each n_ϕ using the fluid approximation ($\omega << \omega_{\rm pe} \sim \omega_{\rm ce}$) [28]. Approximately, the result can be expressed in the following equations (SI units)

$$n_{\rm e1} \approx -\frac{i}{\omega} n_{\rm e0} \nabla \cdot \vec{v}_{\rm e1}, \tag{2}$$

where

$$v_{\rm e1,\parallel} \approx \frac{\omega_{\rm ce}}{\omega} \frac{E_\parallel}{B}, \tag{3}$$

and

$$v_{\rm e1,\perp} \approx \frac{E_\perp}{B}. \tag{4}$$

The subscript '1' on electric fields has been dropped for clarity. For the fast wave, which has a negligible $E_\parallel$, the component of the electric field parallel to B field, its contribution to $n_{\rm e1}$ is mainly from the perpendicular field $E_\perp$. For the MC waves, $E_\parallel$ is about two orders of magnitude smaller than $E_\perp$, but the contribution from $E_\parallel$ is often comparable or larger because of the factor $\omega_{\rm ce}/\omega \sim m_{\rm i}/m_{\rm e}$. The total density fluctuation is the sum of $n_{\rm e1}(n_\phi)$ weighted by the antenna current spectrum $j(n_\phi)$ and $R_{\rm L}(n_\phi)$,

$$n_{\rm e1} = \sum_{n_\phi=-20}^{20} n_{\rm e1}(n_\phi) j(n_\phi) e^{i n_\phi \Delta\phi} \sqrt{\frac{P_{\rm RF}}{R^{\rm tot}_{\rm L}}} \tag{5}$$

where $P_{\rm RF}$ is the total RF input power, $\Delta\phi = 216^{\rm o}$ is the toroidal angle from the center of J-antenna to the PCI chords, and the total coupling resistance

$$R^{\rm tot}_{\rm L} = \sum_{n_\phi=-20}^{20} |j(n_\phi)|^2 R_{\rm L}(n_\phi). \tag{6}$$

The PCI measurement is modeled as the line integral of this 2-D $n_{\rm e1}$ along 32 vertical chords. The finite detector element size imaged into the plasma is modeled as a simple average over a width about 0.4 cm. Equation (6) is also used to obtain the power deposition profile from

TORIC. For example, the power deposition profile from mode conversion is calculated as

$$S^{\rm mc}_{\rm toric}(\rho) = \sum_{n_\phi=-20}^{20} |j(n_\phi)|^2 S^{\rm mc}_{\rm toric}(n_\phi,\rho)\frac{P_{\rm RF}}{R^{\rm tot}_{\rm L}}, \tag{7}$$

which can be compared with the experimental result from Eq. (1).

III. RESULTS

Using the experimental PCI and synthetic PCI, we have studied the influences on the mode conversion of the species mix, MC layer location, and $B_{\rm pol}/B_{\rm tot}$. The results are presented in the following two Sections – off axis and near axis – based on the MC layer location relative to the magnetic axis. In each Section, discharges at two different B fields and RF frequencies are also compared.

A. Off axis mode conversion

In Fig. 4, we show the PCI data of a discharge where the mode conversion is off axis on the LFS. In this figure, the PCI line integrated fluctuations caused by the RF waves are plotted vs. major radius and time. The input RF power is also plotted. The plasma parameters are $I_{\rm p} = 1.0$ MA, $n_{\rm e0} = 2.0\times10^{20}$ m^{-3}, $T_{\rm e0} = 2.1$ keV and $T_{\rm i} \simeq T_{\rm e}$, $n_{\rm H}/n_{\rm D} = 4\%$, $R_{\rm axis} = 0.683$ m and $B_{\rm axis} = 5.57$ T. The RF frequency $f_{\rm RF} = 50$ MHz. ^{3}He gas is puffed for 150 ms from $t = 0.3$ to $t = 0.45$ sec. A peak is clearly shown in the PCI signal around $R = 0.72 - 0.73$ m when the RF is on. The peak moves to the LFS by about 1 cm in time. This can be explained by the slow depletion of ^{3}He ions in the plasma during the discharge. In Fig. 5, we plot the power deposition profiles from TORIC simulations at different ^{3}He levels and also compare with the experimental curve, which is calculated from the break in slope in $T_{\rm e}$ signals at the RF shut-off at $t = 1.08$ sec. The TORIC curve of $n_{^3{\rm He}}/n_{\rm e} = 11\%$ matches the experimental curve the best, while the other two TORIC curves differ either in the level or location. The possibility that the MC layer is on the HFS of the axis is excluded by comparing discharges in a B field scan while other parameters are fixed. From the curve of $n_{^3{\rm He}}/n_{\rm e} = 11\%$, TORIC predicts that 37% incident power is absorbed directly by electrons through mode conversion. Figure 5 suggests that we can constrain the uncertainty of the ^{3}He level to be within $\pm1\%$ by matching the power deposition profiles. On the other hand,

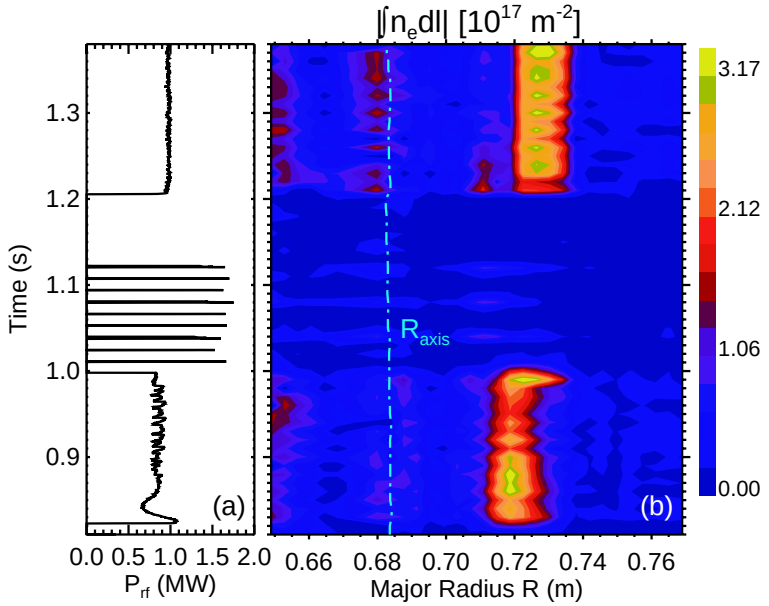

FIG. 4: A discharge with off-axis mode conversion. $f_{\rm RF} = 50$ MHz, $B_{\rm axis} = 5.57$ T, $n_{\rm H}/n_{\rm e} = 3\%$, $n_{\rm D}/n_{\rm e} = 75\%$, $n_{^3{\rm He}}/n_{\rm e} = 11 - 12\%$. (a) RF power vs. time. (b) The PCI measured line-integrated fluctuation level at the beat frequency vs. time and major radius.

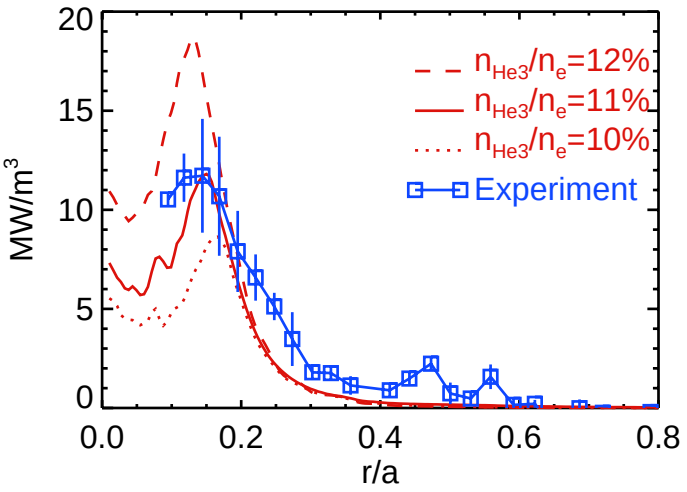

FIG. 5: Comparison of the mode conversion direct electron heating profiles. The experimental curve is calculated from the break-in-slope of $T_{\rm e}$ signals at a fast RF shut-off at $t = 1.08$ sec.

such a constraint also determines the location of the MC layer on the mid-plane to be within ± 0.5 cm. Considering the variation of the peak location in Fig. 4, a value of 12% may be better for the earlier part of the discharge and 10% for the later part of the discharge.

In Fig. 6, we show the 2-D contours of the parallel electric field $E_{||}$ from the TORIC

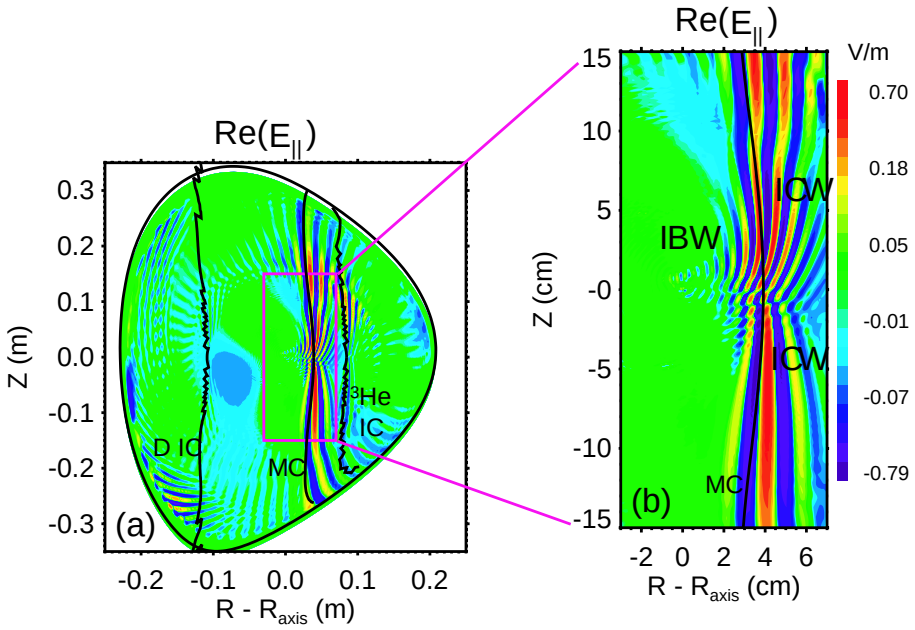

FIG. 6: $E_{\|}$ field from TORIC simulation ($n_\phi = +7$ and 1 A antenna current) at $t = 1.38$ sec of the discharge in Fig. 4. The MC layer, ^{3}He and D resonance layers are also plotted.

simulation of $n_\phi = 7$ for the above discharge at $t = 1.38$ sec. The MC layer (D-^{3}He hybrid layer), D and ^{3}He IC resonance layers are also plotted. The field is plotted in logarithmic scale so that all ICRF waves are shown. There are two different short wavelength structures on the HFS and LFS of the MC layer respectively. On the HFS, it is the MC IBW and on the LFS, it is the MC ICW. In Fig. 7, the 2-D contours of the density fluctuations caused by the RF wave are plotted (also in logarithmic scale), which shows the MC waves are the major contributors to the density fluctuations, while the fast wave contribution is insignificant. We then do line integration of n_{e1} along the vertical PCI chords, do summation using Eq. (5), and compare the result with the experimental PCI (Fig. 8). Excellent agreement between experimental data and synthetic output is shown in the structure of both real and imaginary parts of the line integrated density fluctuations. Spatially damped wave structures with wavelength in the order of 1 cm are present on both sides of the MC layer. In Fig. 8-(c), a full width at half maximum (FWHM) about 2 cm is shown in the fluctuation level. We also compare the $k_{\rm R}$ spectra in Fig. 9. Both experimental PCI and synthetic PCI show a broad peak at $k_{\rm R} = 3 - 6$ cm^{-1}. A positive $k_{\rm R}$ indicates that the wave phase velocity is toward the LFS. Such a $k_{\rm R}$ spectrum is expected from the 2-D plot in Fig. 7, which shows similar wavelengths for the IBW and ICW near the MC layer. To further show the local

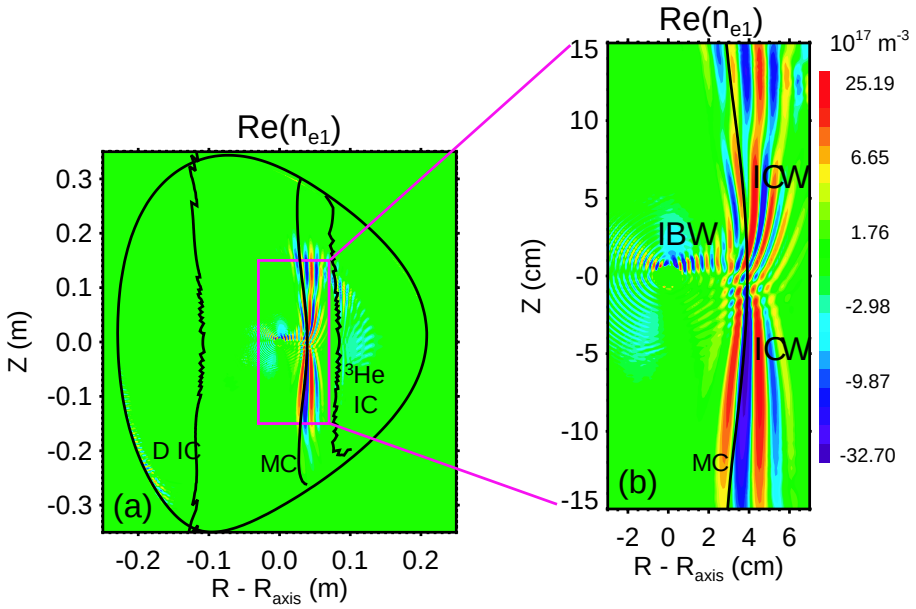

FIG. 7: Two-dimensional density fluctuations calculated by the synthetic PCI ($n_\phi = +7$).

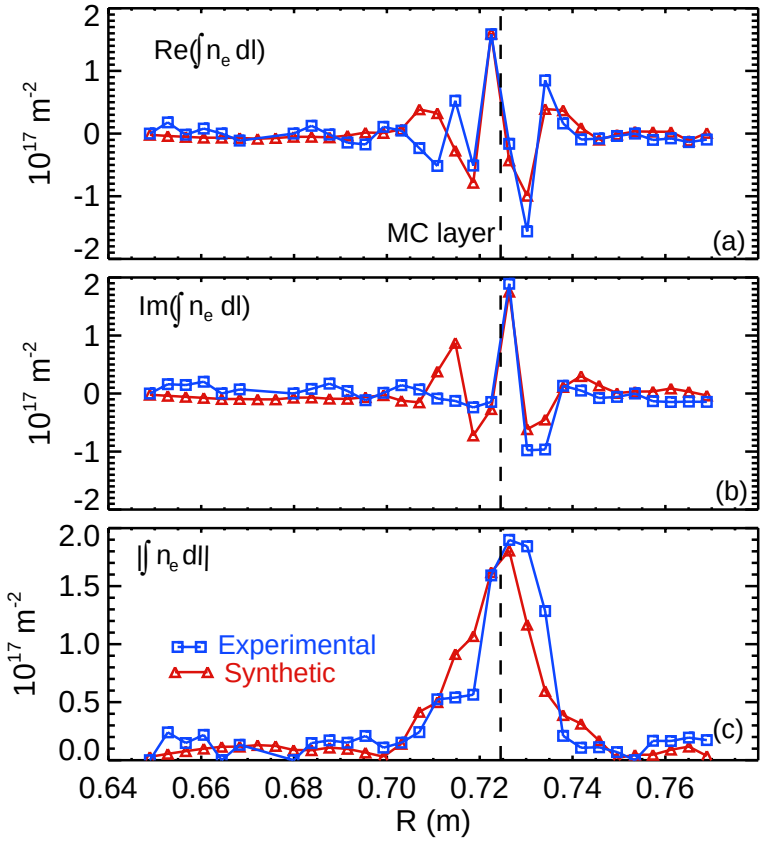

FIG. 8: Experimental and synthetic PCI line integrated density fluctuations for the discharge in Fig. 4: (a) real part, (b) imaginary part, (c) magnitude.

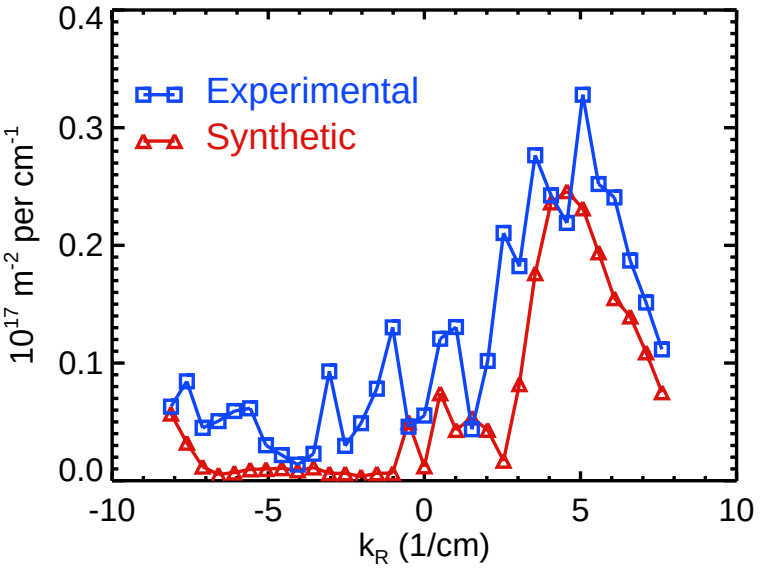

FIG. 9: k_{R} spectra of the experimental and synthetic PCI line integrated density fluctuations of the discharge in Fig. 4.

wave structure, we plot k_{loc} calculated from the phase information between PCI channels in Fig. 10-(a) and compare it with the dispersion curves in Fig. 10-(b). In the region where the PCI signals are large, k_{loc} is close to $4-5$ cm^{-1} for both experimental PCI and synthetic PCI, in agreement with the spectrum shown in Fig. 9. In contrast to the dispersion curves in Fig. 10-(b), there is no sudden change in k_{loc} in the MC region in both experimental and synthetic k_{loc} curves. Neither is there a rapid increase of the IBW wavenumber toward the HFS. Instead, Fig. 10-(a) shows that about $1-2$ cm away from the MC layer, k_{loc} decreases rapidly. This apparent discrepancy can be explained by the line integration nature of the PCI measurement and also the 2-D structure of the MC waves. First, the MC layer is not a vertical line (see Figs. 6 and 7), and it is more curved near the mid-plane due to finite β_{p}, the ratio of plasma pressure and poloidal magnetic field pressure. Moreover, the MC locations are slightly different for different n_ϕ. Secondly, in locations away from the MC layer, the fast wave level becomes comparable or even greater than either the MC ICW or MC IBW, which are more heavily damped. As shown in Fig. 8-(a) and (b), about 2 cm away from the MC layers, the long wavelength FW gradually dominate the PCI measurements. k_{loc} is sensitive to this ratio of FW and MC waves. The difference in the two k_{loc} curves on the HFS of the MC layer shown in Fig. 10-(a) is due to a small difference in the ratios of FW and IBW in the experimental PCI and synthetic PCI. In all, the PCI observation can rarely reproduce

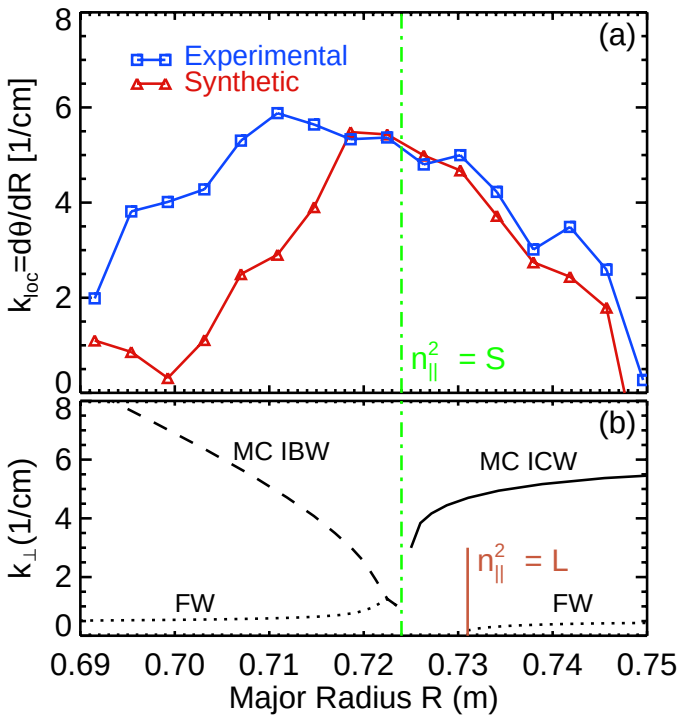

FIG. 10: (a) Local wave number $k_{\rm loc} = d\theta/dR$ from experimental measurements and synthetic PCI. (b) Dispersion curves. IBW and FW are calculated from the mid-plane, while the ICW is calculated along the magnetic surface. The MC layer $n_\parallel^2 = S$ and the left cutoff layer $n_\parallel^2 = L$ is also plotted. L is the usual Stix' notation [15].

the local structure in the dispersion curves shown in Fig. 10-(b), which may only be possible using a diagnostic with sufficient spatial localization capability and k-space filtering.

The experimental PCI observations of off axis mode conversion in B $\sim$ 8 T and $f_{\rm RF}$ = 78 MHz are similar. In Fig. 11, we show the PCI data in such a discharge. The plasma parameters are $B_{\rm axis}$ = 7.81 T, $I_{\rm p}$ = 1.2 MA, $n_{\rm e0} = 2.1 \times 10^{20}$ m^{-3}, $T_{\rm e0}$ = 4.1 keV and $T_{\rm i} \simeq T_{\rm e}$, $n_{\rm H}/n_{\rm D} = 5\%$. The ^{3}He puff time is the same as the discharge in Fig. 4. We use $n_{^3{\rm He}}/n_{\rm e} \simeq 12\%$ for TORIC simulations. In Fig. 12, the experimental PCI and synthetic PCI are compared. Good agreement is also shown in the real part, imaginary part and magnitude of the fluctuations. Similar to Fig. 8, short wavelength wave structures exist on both sides of the MC layer. Fig. 13 shows the $k_{\rm R}$ spectra of the experimental PCI and the synthetic PCI. The MC waves are shown as a broad peak at $k_{\rm R} \sim 3 - 5$ cm^{-1} in both spectra similar to that in Fig. 9.

The 2-D structure of the MC waves is different due to the smaller $B_{\rm pol}/B_{\rm tot}$ in this

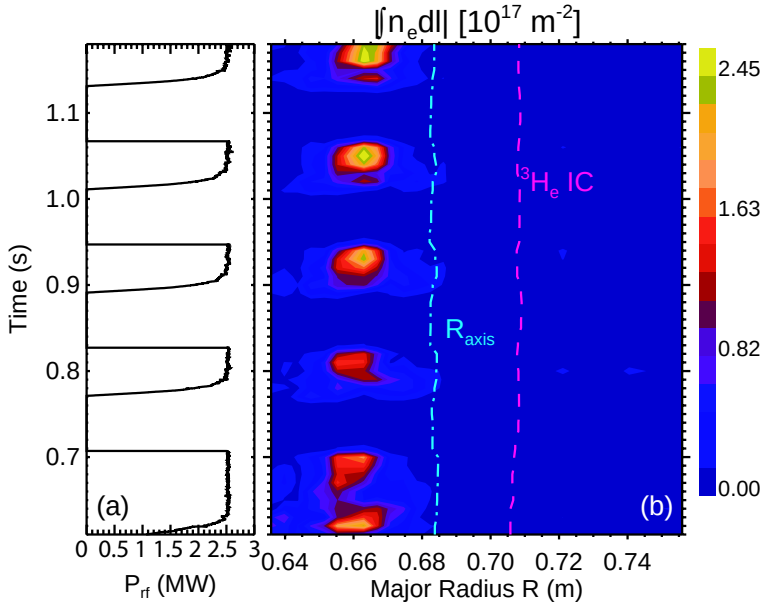

FIG. 11: A discharge with off-axis mode conversion. $f_{\rm RF} = 78$ MHz, $B_{\rm axis} = 7.81$ T, $n_{\rm H}/n_{\rm e} = 5\%$, $n_{\rm D}/n_{\rm e} = 72\%$, $n_{^3{\rm He}}/n_{\rm e} = 12\%$. (a) RF power vs. time. (b) The PCI measured line-integrated fluctuation level vs. time and major radius.

discharge. In Fig. 14 we show the contour of the density fluctuations from the synthetic PCI ($n_\phi = 7$). Unlike in Fig. 7, the MC ICWs in both upper and lower planes start to propagate significantly farther away from the mid-plane. The wave number of a wave can undergo transformation along the wave path following the approximate equation,

$$k_\parallel \approx \frac{n_\phi}{R}\frac{B_\phi}{B_{\rm tot}} + \frac{m}{r}\frac{B_{\rm pol}}{B_{\rm tot}}, \tag{8}$$

where m is the poloidal mode number. m is not conserved along the wave path. The ICW only exists where the up-shift of $k_\parallel$ in Eq. (8) is significant. This condition cannot be fulfilled when $B_{\rm pol}/B_{\rm tot} \ll 1$, e.g., near the magnetic axis. The term $B_{\rm pol}/B_{\rm tot}$ in Eq. (8) of this discharge is smaller than that of the discharge in Fig. 4. As a result, the mode conversion to the ICW occurs in locations farther away from the mid-plane. It is worth pointing out that the MC ICW above the mid-plane appears at $Z \geq 10$ cm, while the ICW below the mid-plane appears at about $Z \simeq -4$ cm for this $n_\phi = +7$. Such asymmetry can also be explained by Eq. 8. Note for a wave propagating toward the LFS, it has $m < 0$ above the mid-plane and $m > 0$ below the mid-plane. To have a large $|k_\parallel|$, a larger 2nd term in Eq. (8) is required for $m < 0$ than for $m > 0$. Such a requirement makes the mode conversion to ICW more favorable below (above) the mid-plane for $n_\phi > 0$ ($n_\phi < 0$).

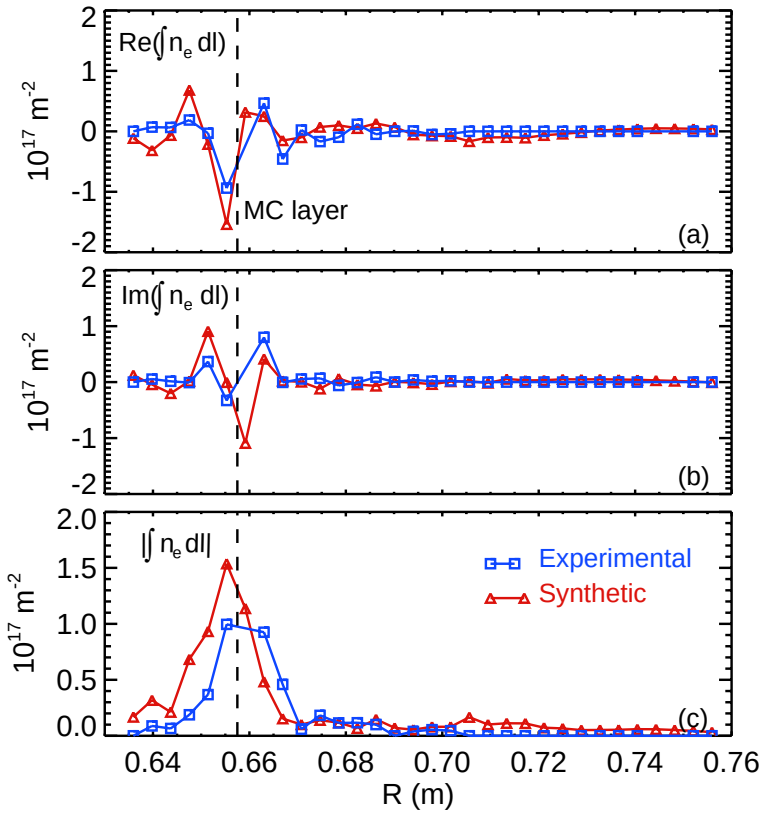

FIG. 12: Experimental and synthetic PCI line integrated density fluctuations for the discharge in Fig. 11: (a) real part, (b) imaginary part, (c) magnitude.

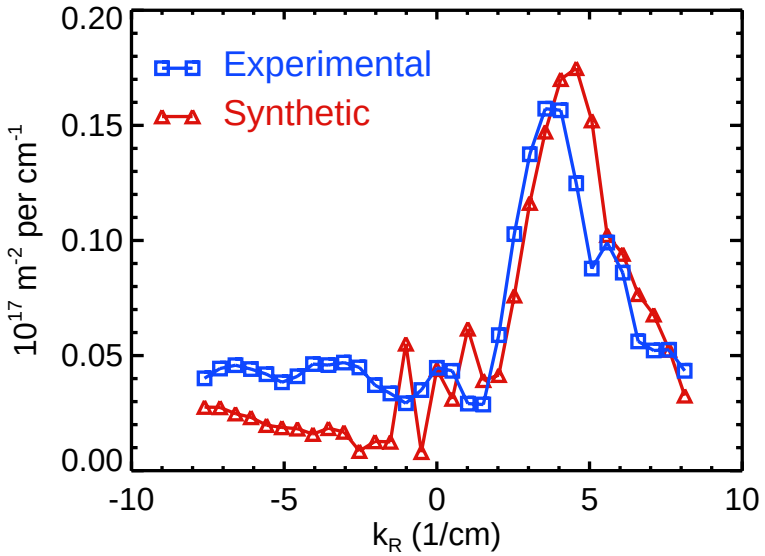

FIG. 13: k_{R} spectra of the experimental and synthetic PCI line integrated density fluctuations of the discharge in Fig. 11.

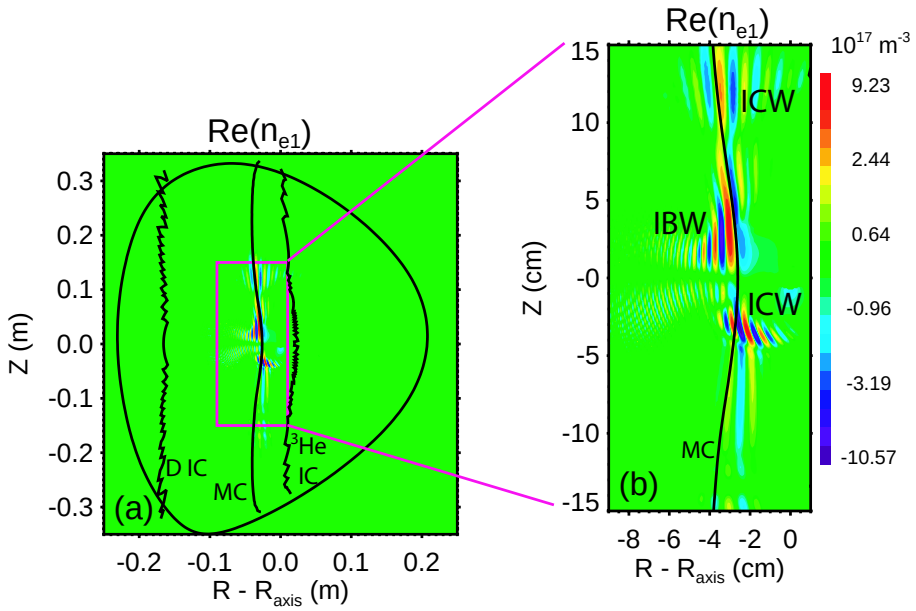

FIG. 14: Two-dimensional density fluctuations calculated by the synthetic PCI for the discharge in Fig. 11. The MC layer, ^{3}He and D resonance layer are also plotted. $R_{\rm axis} = 0.682$ m.

In summary, when the MC layer is off axis, the PCI diagnostic has observed spatially damped short wavelength waves on both sides of the MC layer. The experimental result is in good agreement with the synthetic PCI result. The two MC waves are clearly distinguishable as the MC IBW and MC ICW in TORIC simulations.

B. Near axis mode conversion

In Fig. 15, we show a discharge with same parameters as that in Fig. 4, except a lower B field ($B_{\rm axis} = 5.41$ T). The structure of the MC waves in PCI moves toward a smaller major radius accordingly. Interestingly, the broad single peak in Fig. 4 is split into two distinct peaks. The dip between these two peaks also evolves during the discharge. This double hump structure in PCI measurements appears in several discharges where the MC layer is near the axis. The dip can appear in different channels, which rules out the possibility of a bad PCI channel. In Fig. 16, we compare the experimental result with the synthetic PCI output ($n_{^3\rm He}/n_{\rm e} = 12\%$). The real and imaginary part of the density fluctuations both show short wavelength waves on both sides of the MC layer. The synthetic PCI also has a double hump structure as seen in Fig. 16-(c), which shows the magnitude of the fluctuations. The

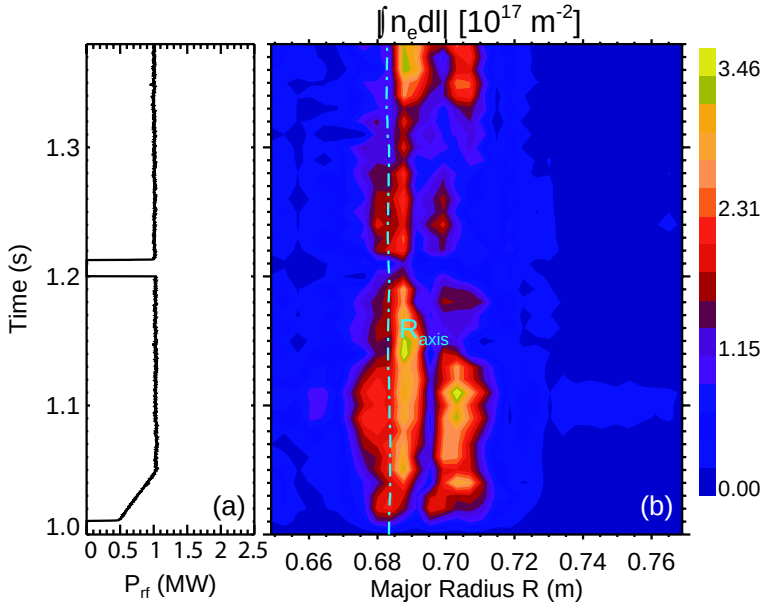

FIG. 15: A discharge with near axis mode conversion. $f_{\rm RF} = 50$ MHz, $B_{\rm axis} = 5.41$ T, $n_{\rm H}/n_{\rm D} = 4\%$, $n_{^3{\rm He}}/n_{\rm e} = 11 - 12\%$. (a) RF power vs. time. (b) The PCI measured line-integrated fluctuation level vs. time and major radius.

dip of the double hump structure is close to the MC layer.

The double hump structure is the result of up-down asymmetry in wavelength of the MC ICWs above and below the mid-plane. In Fig. 17, the contours of the 2-D density fluctuation from TORIC simulation of $n_\phi = 6$ is plotted. The vertical dashed line in Fig. 17-(b) indicates a PCI chord. It is clearly shown that the ICWs above the mid-plane and below the mid-plane are canceled out along this chord, while the cancellation is smaller in other locations. The wavelengths of the MC ICW above and below the mid-plane are different, which can be estimated from Eq. (8). For two locations with the same vertical $|Z|$ above and below the mid-plane, $k_\perp \sim m/r$ should differ approximately,

$$|\Delta k_\perp| \approx 2\frac{n_\phi}{R}\frac{B_\phi}{B_{\rm pol}}, \tag{9}$$

to have a similar $|k_\parallel|$ to meet the local dispersion equation. To show in more detail, in Fig. 18 we plot $\rm B_{pol}$ contours from EFIT with the density fluctuations from Fig. 17. Two up-down pairs of ICW are selected and approximate wavelengths, $\lambda \simeq \lambda_\perp$, are calculated. The differences in $k_\perp$ are also labeled in the figure. Using $n_\phi = 6$ and $B_{\rm axis} = 5.41$ T, equation (9) gives $|\Delta k_{\perp 1}| \simeq 3.1$ cm^{-1}, and $|\Delta k_{\perp 2}| \simeq 3.6$ cm^{-1}, respectively. These values are in good agreement with $|\Delta k_{\perp 1}| \simeq 3.5$ cm^{-1} and $|\Delta k_{\perp 2}| \simeq 3.8$ cm^{-1} shown in the figure.

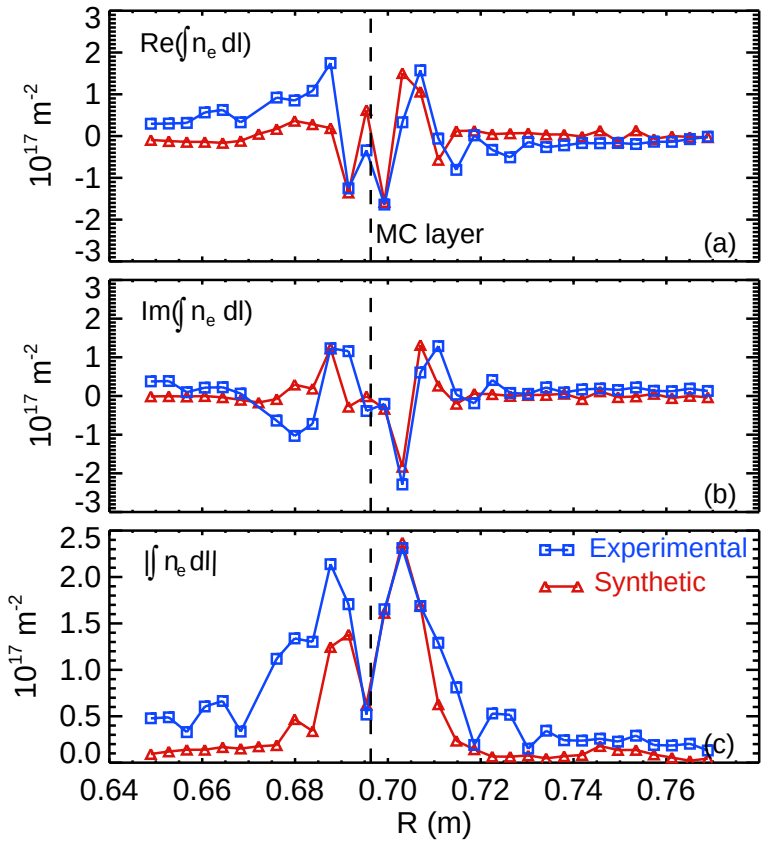

FIG. 16: Experimental and synthetic PCI line integrated density fluctuations amplitude vs. major radius for the discharge in Fig. 15. (a) real part, (b) imaginary part, (c) magnitude.

This agreement suggests that the double hump structure results from the interference pattern between the MC ICWs above and below the mid-plane. At a smaller B_{pol} (near the axis), this pattern is more prominent because the up-down asymmetry in wave number is stronger according to Eq. (9). Such asymmetry in wavelength is smaller when the MC layer is off axis (cf. Fig. 7). Equation (9) is not applicable for cases like that in Fig. 14, where ICWs are at different $|Z|$.

In Fig. 19 we compare the k_R spectrum of the PCI measurements and the synthetic PCI output. There are three peaks in both spectra. The one near $k \simeq \pm 0.5$ cm^{-1} is the fast wave, which is in agreement with the expected FW wave number (cf. Fig. 10-(b)). The peak at $k_R \simeq -0.5$ cm^{-1} is larger than the one at $k_R \simeq +0.5$ cm^{-1}, suggesting that the inward propagating fast wave has a larger amplitude than the outward propagating fast wave. This observation indicates that the fast wave field in the plasma does not appear as a standard standing-wave pattern. Because of the mode conversion to the MC ICW, the left cutoff

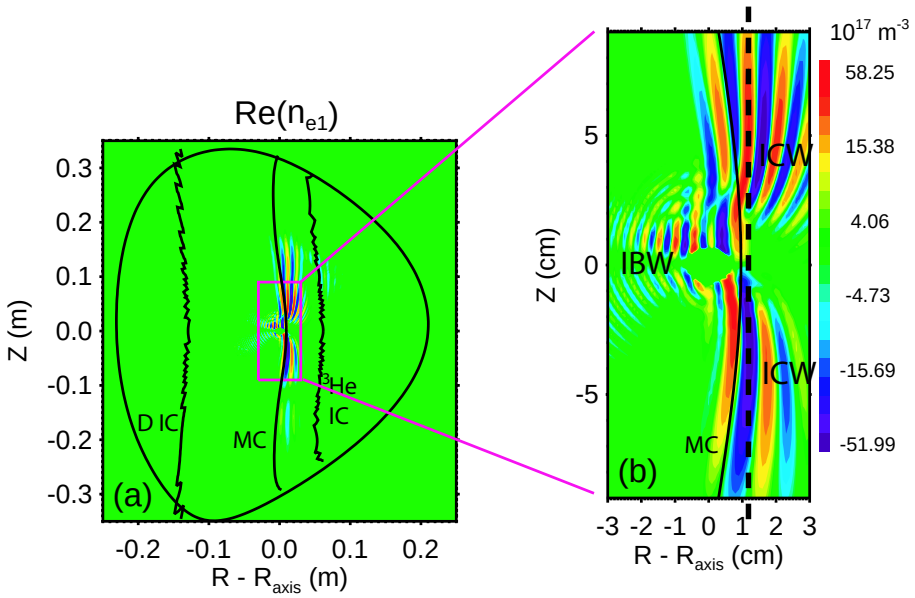

FIG. 17: Two-dimensional density fluctuations calculated by the synthetic PCI ($n_\phi = 6$). The vertical dashed line in figure (b) indicates a PCI chord.

layer $n_{||}^2 = L$ (e.g. Fig. 10-(b)) no longer acts as a reflection layer for the fast waves reflected from the right cutoff layer $n_{||}^2 = R$ at the HFS edge. The resulting fast wave pattern is more like a wave with a load in one end. There are two other broad peaks in Fig. 19 at $k \sim 3$ cm^{-1} and $k \sim 8$ cm^{-1}. Both are definitely from the MC waves. However, more detailed analysis finds that neither peak is solely from the MC IBW nor solely from the MC ICW. In Fig. 20, we show the result of Fourier transformations of the synthetic PCI output done separately on channels at $R < 0.69$ m and channels at $R > 0.69$ m (zeroing-out the remaining channels). Note that the spectrum for all 32 channels is the linear combination of these two complex spectra. The spectra in Fig. 20-(a) are broad, comparable to those in Figs. 9 and 13. The phase difference of these two complex spectra, shown in Fig. 20-(b), approaches π at $k_R \sim 4$ cm^{-1}. The destructive combination of these two spectra at $k_R \sim 4$ cm^{-1} can explain the double peak structure in the k_R spectra shown in Fig. 19. The ambiguity in interpreting the simple k_R spectrum of Fig. 19 is caused by the fact that multiple waves with similar k_R exist in a narrow MC region.

The near axis mode conversion at ~ 8 T is different than the one at ~ 5.4 T. In these discharges, the MC IBW is found to be the only MC wave. In Fig. 21, we show the PCI data of such a discharge at $B_\mathrm{axis} = 7.73$ T and $f_\mathrm{RF} = 78$ MHz. The MC signals appear at

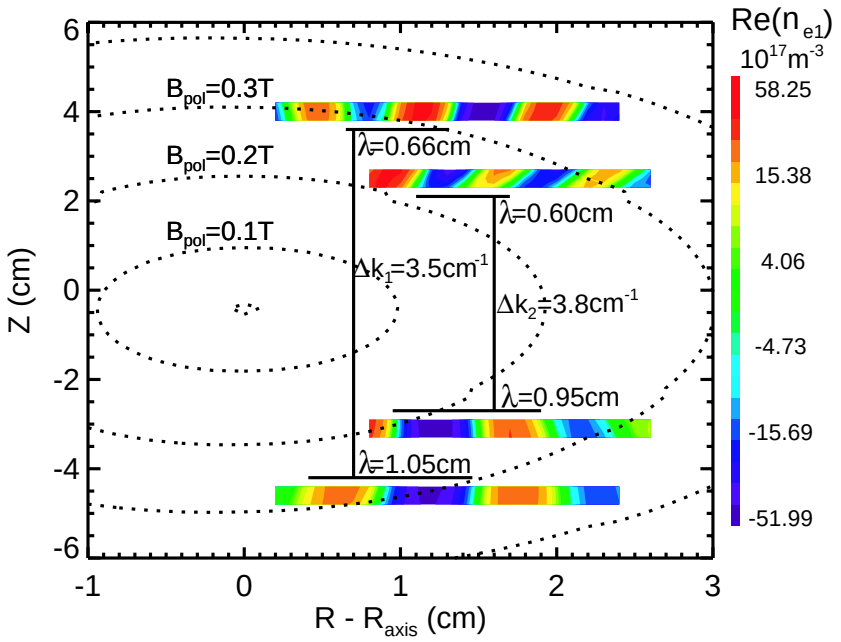

FIG. 18: MC ICW up-down asymmetry and B_{pol}. Dot lines are B_{pol} contours, while color contours are density fluctuations.

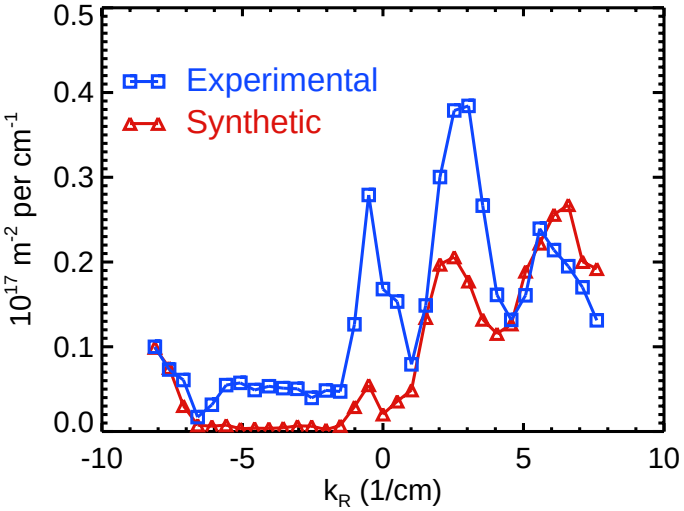

FIG. 19: k_{R} spectra of the experimental and synthetic PCI line integrated density fluctuations for the discharge in figure 15.

around $R = 0.66 - 0.67$ m. Other plasma parameters are $I_{\mathrm{p}} = 1.2$ MA, $n_{\mathrm{e0}} = 2.1 \times 10^{20}$ m^{-3}, $T_{\mathrm{e0}} = 4.1$ keV and $T_{\mathrm{i}} \simeq T_{\mathrm{e}}$, $n_{\mathrm{H}}/n_{\mathrm{D}} = 5\%$. $R_{\mathrm{axis}} = 0.682$ m. ^{3}He gas was puffed only for 50 ms in the discharge. The ^{3}He concentration is estimated to be $n_{^3\mathrm{He}}/n_{\mathrm{e}} = 5\%$ by comparing to the TORIC simulations.

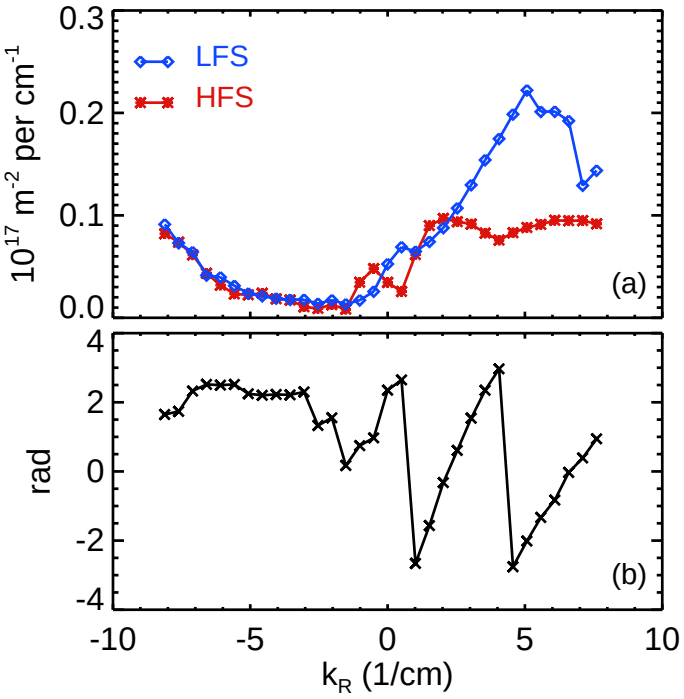

FIG. 20: k_{R} spectra calculated in two separate regions: (a) magnitude, (b) phase difference of the two spectra.

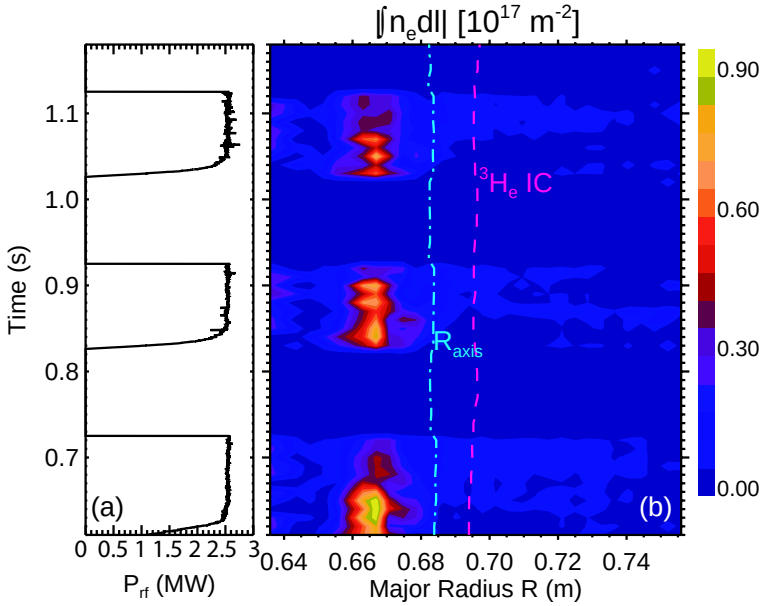

FIG. 21: A discharge with on-axis mode conversion. $f_{\mathrm{RF}} = 78$ MHz, $B_{\mathrm{axis}} = 7.73$ T, $n_{\mathrm{H}}/n_{\mathrm{D}} = 5\%$, $n_{^3\mathrm{He}}/n_{\mathrm{e}} = 5\%$. (a) RF power vs. time. (b) The PCI measured line-integrated fluctuation level vs. time and major radius.

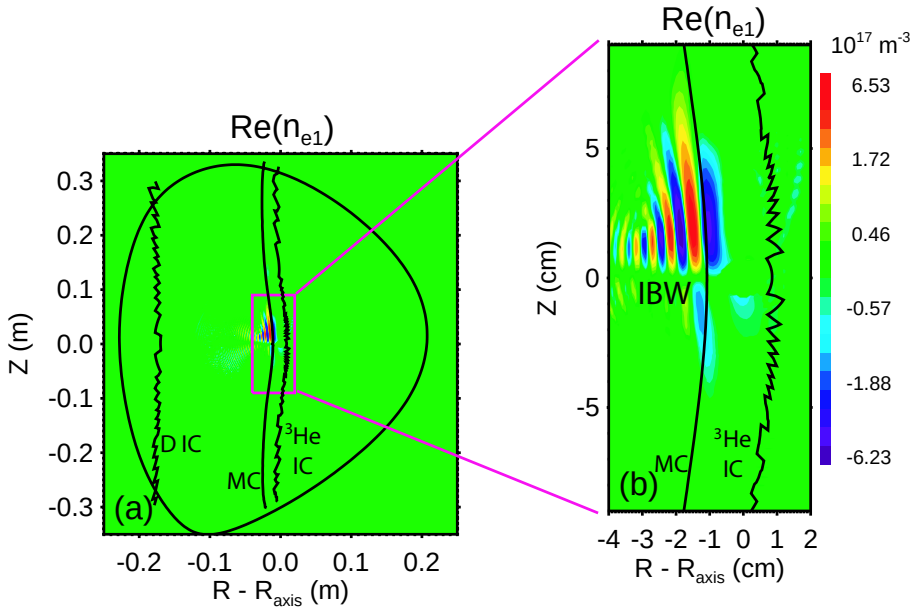

FIG. 22: Density fluctuations in 2-D calculated by the synthetic PCI for the discharge in Fig. 21 ($t = 0.64$ sec).

For this discharge, the MC IBW is the only MC wave as seen in Fig. 22, in which the density fluctuations is plotted from the TORIC simulation of $n_\phi = 7$. Since $B_{\rm pol}/B_{\rm tot} \ll 1$, mode conversion to IBW dominates. In Fig. 23, the experimental PCI data is compared with the synthetic PCI data vs. major radius. The short wavelength wave structure is mostly on the HFS of the MC layer (note the MC layer indicated in the figure is from cold plasma approximation). The detectors in the PCI system are sensitive to wave numbers up to $k_{\rm lim} \simeq 17$ cm^{-1}, larger than the maximum $k_{\rm R}$ determined by the channel separation, $k_{\rm max} \simeq 8$ cm^{-1}. As a result, waves having $k_{\rm max} \le k_{\rm R} \le k_{\rm lim}$ may be also detected by the PCI, but appear in the PCI spectrum at $k_{\rm R} - 2k_{\rm max}$ due to spatial aliasing. In Figs. 24-(a) and (b), we plot the $k_{\rm R}$ spectra from both experimental PCI and synthetic PCI. There is a broad peak at $k_{\rm R} < -3$ cm^{-1} in Fig. 24-(a). To check whether this part of the spectrum is aliased, we double the total channel number and reduce the separation between channels by half in the synthetic PCI, and calculate the $k_{\rm R}$ spectrum again. The broad peak at $k_{\rm R} < -3$ cm^{-1} in the synthetic PCI spectrum indeed disappears. Instead, the peak at positive $k_{\rm R}$ is extended to $k_{\rm R} \sim 13$ cm^{-1} as shown in Fig. 24-(b). This result demonstrates that 32 channel PCI does not have adequate spatial resolution for the MC IBW, resulting in spatial aliasing in the $k_{\rm R}$ spectrum. Assuming the part at $k_{\rm R} < -3$ cm^{-1} of the experimental PCI spectrum is all

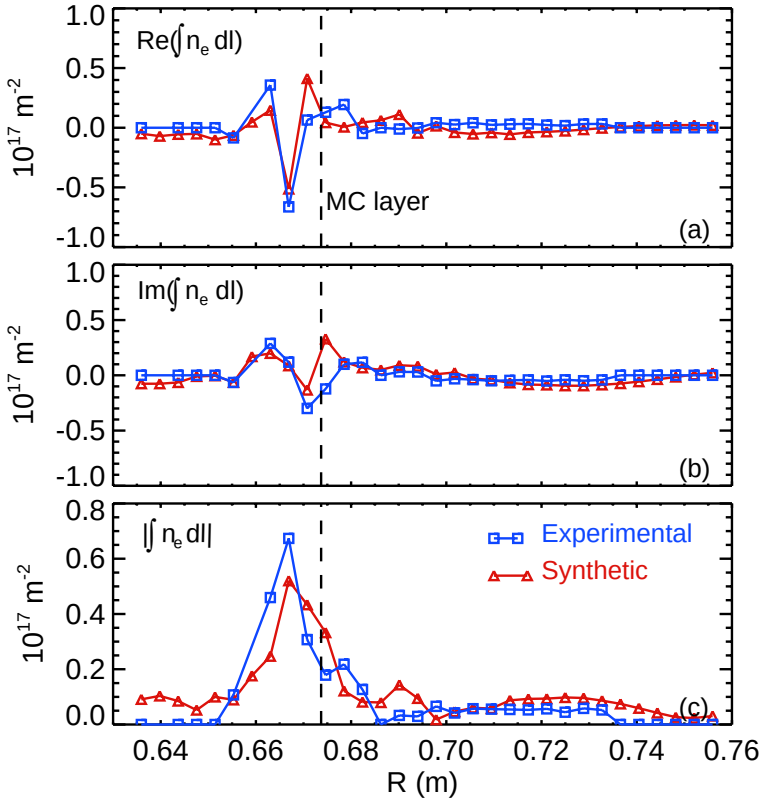

FIG. 23: Experimental and synthetic PCI line integrated density fluctuations amplitude vs. major radius for the discharge in Fig. 21. (a) real part, (b) imaginary part, (c) magnitude.

aliased and shifting it by $2k_{\max}$, we also find a broad MC IBW peak from $k_{\rm R} = 2$ to 13 cm^{-1} as shown in Fig. 24-(b), in good agreement with the one from the 64 channel synthetic PCI. There are also fast wave peaks at $k_R \simeq \pm 0.5$ cm^{-1} in this figure. In Fig. 25, we plot the dispersion curves for the IBW and fast wave. The dispersion curve of the MC IBW shows that it has the same range of wave number as in Fig. 24-(b). No MC ICW root exists along the magnetic surface tangential to the MC layer. This is the first definitive observation of IBW-only mode conversion by PCI in Alcator C-Mod.

In summary, PCI observations of the near axis mode conversion at 50 MHz show both the MC IBW and MC ICW. The fast wave has also been observed in some discharges. The up-down asymmetry of the MC ICW, which is more prominent in near axis mode conversion than off axis, creates a double hump interference structure, seen in both experiments and simulations. In 8 T near axis mode conversion, the MC IBW is shown to be the only MC wave because of a small $B_{\rm pol}/B_{\rm tot}$. The experimental $k_{\rm R}$ spectrum of the MC IBW agrees with the synthetic PCI and dispersion curve after spatial aliasing is considered.

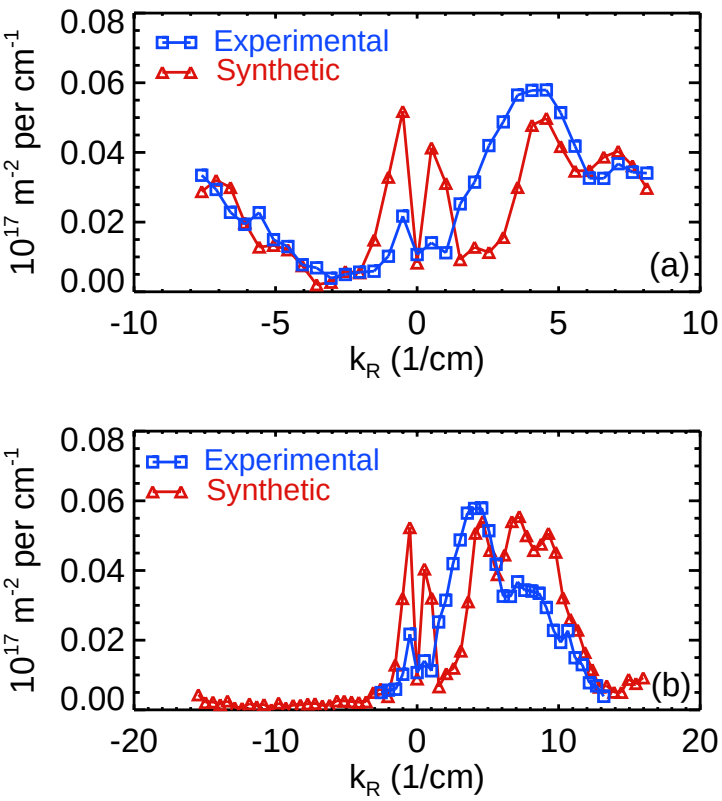

FIG. 24: k_R spectra of the experimental and synthetic PCI line integrated density fluctuations for the discharge in Fig. 21. (a) Usual spectra. (b) All $k_R < 3$ cm^{-1} in the experimental PCI spectrum are shifted by 16 cm^{-1}, while the synthetic PCI has twice the number of channels of the experimental PCI.

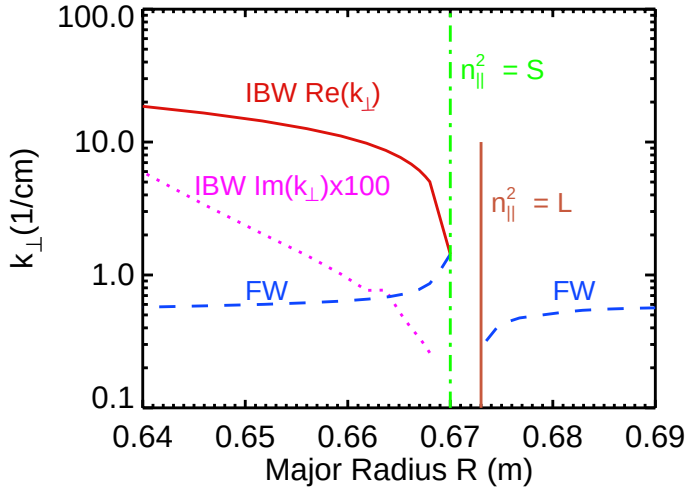

FIG. 25: Dispersion curves of IBW and FW calculated at the mid-plane. Both the imaginary and real parts of the MC IBW are shown.

IV. DISCUSSION AND FUTURE WORK

The experimental PCI and synthetic PCI agree very well after multiplying by the correction factors as mentioned in Sec. II B. We hypothesize that the absolute calibration of the heterodyne scheme of PCI is the likely explanation. And the calibration needs to be improved. The issues to be resolved include the calibration of the detector responses in the MHz frequency range and the laser modulation efficiency of the AOMs. The up-down asymmetry of the MC ICW can explain the double hump structure seen in the PCI measurement in 50 MHz near axis mode conversion and is also clearly shown in the TORIC simulation. However, because of the line integration nature of the present PCI diagnostic, the up-down asymmetry was not measured directly. In the future, the PCI system will be upgraded to have the capability of vertical spatial localization [29]. After this upgrade, we may be able to experimentally study the mode conversion region in 2-D. The MC IBW spectrum in 78 MHz near axis MC discharges has a problem of spatial aliasing. By reducing the separation between the channels, we may be able to obtain the MC IBW spectrum without aliasing ambiguity.

V. SUMMARY

ICRF waves on multiple spatial scales in the mode conversion region of D(^{3}He) plasmas have been observed using PCI in the Alcator C-Mod tokamak. Good agreement has been obtained between the experimental observation and the result of a synthetic PCI based upon TORIC. The observed waves include the fast wave, MC ICW and MC IBW. When the mode conversion layer is off-axis, both MC IBW and MC ICW were observed. In near axis mode conversion discharges at $B \sim 5.4$ T ($f_{\mathrm{RF}} = 50$ MHz), a double hump structure was observed experimentally and reproduced by the synthetic PCI. Such structure is an indication of the up-down asymmetry of the MC ICW. The MC IBW has been shown to be the only MC wave in near axis mode conversion discharges at $B \sim 8$ T ($f_{\mathrm{RF}} = 78$ MHz). This work is the first comprehensive experimental and numerical study of ICRF wave phenomena in the mode conversion region of Alcator C-Mod.

Acknowledgments

The authors thank RF engineer Mr. C. Schwartz, who died in a plane crash in October 2004, for his substantial contribution to the ICRF system operation. Many thanks also go to Dr. E. Nelson-Melby and Mr. K. Jordy in the development of the synthetic PCI. This research utilized the MIT Plasma Science and Fusion Center Theory Group parallel computational cluster. This work is supported at MIT by U.S. DoE Cooperative Agreement No. DE-FC02-99ER54512.

---

[1] M. Porkolab. Plasma heating by fast magnetosonic waves in tokamaks. In N. Fisch, editor, *Advances in Plasma Physics*, volume 314 of *AIP Conference Proceedings*, page 99, New York, 1994. American Institute of Physics.

[2] F. W. Perkins. Heating tokamaks via the ion-cyclotron and ion-ion hybrid resonances. *Nucl. Fusion*, 17(6):1197, 1977.

[3] E. Nelson-Melby, M. Porkolab, P. T. Bonoli, Y. Lin, A. Mazurenko, and S. J. Wukitch. Experimental observations of mode-converted ion cyclotron waves in a tokamak plasma by phase contrast imaging. *Phys. Rev. Lett.*, 90(15):155004, 2003.

[4] E. F. Jaeger, L. A. Berry, J. R. Myra, et al. Sheared poloidal flow driven by mode conversion in tokamak plasmas. *Phys. Rev. Lett.*, 90(19):195001, 2003.

[5] Y. Lin, S. J. Wukitch, P. T. Bonoli, E. Nelson-Melby, M. Porkolab, J. C. Wright, N. Basse, A. E. Hubbard, J. Irby, L. Lin, E. S. Marmar, A. Mazurenko, D. Mossessian, A. Parisot, J. Rice, and S. Wolfe. Investigation of ion cyclotron range of frequencies mode conversion at the ion-ion hybrid layer in Alcator C-Mod. *Phys. Plasmas*, 11(5):2466, 2004.

[6] J. C. Wright, P. T. Bonoli, M. Brambilla, F. Meo, E. D'Azevedo, D. B. Batchelor, E. F. Jaeger, L. A. Berry, C. K. Phillips, and A. Pletzer. Full wave simulations of fast wave mode conversion and lower hybrid wave propagation in tokamaks. *Phys. Plasmas*, 11(5):2466, 2004.

[7] Y. Lin, S. J. Wukitch, P. T. Bonoli, et al. Ion cyclotron range of frequencies mode conversion electron heating in deuterium-hydrogen plasmas in the Alcator C-Mod tokamak. *Plas. Phys. Control. Fusion*, 45(6):1013, 2003.

[8] M. J. Mantsinen, M.-L. Mayoral, D. Van Eester, et al. Localized bulk electron heating with

ICRF mode conversion in the JET tokamak. *Nucl. Fusion*, 44(1):33, 2004.

[9] B. Saoutic, A. Bécoulet, T. Hutter, A. K. Ram, and A. Bers. Mode conversion heating experiments on the Tore Supra tokamak. *Phys. Rev. Lett.*, 76(10):1647, 1996.

[10] P. T. Bonoli, M. Brambilla, E. Nelson-Melby, et al. Mode conversion electron heating in Alcator C-Mod: Theory and experiment. *Phys. Plasmas*, 7(5):1886, 2000.

[11] P. T. Bonoli, P. O'Shea, M. Brambilla, et al. Electron heating via mode converted ion Bernstein waves in the Alcator C-Mod tokamak. *Phys. Plasmas*, 4(5):1774, 1997.

[12] R. Majeski, J. H. Rogers, S. H. Batha, et al. Ion cyclotron range of frequency experiments in the tokamak fusion test reactor with fast waves and mode converted ion Bernstein waves. *Phys. Rev. Lett.*, 5(76):764, 1996.

[13] S. Wukitch, Y. Lin, A. Parisot, J. C. Wright, et al. Ion cyclotron range of frequency mode conversion physics in Alcator C-Mod: experimental measurements and modeling. *Phys. Plasmas*, 2005, accepted for publication.

[14] C. K. Phillips, M. G. Bell, R. E. Bell, et al. ICRF heating and profile control techniques in TFTR. *Nucl. Fusion*, 40(3Y):461, 2000.

[15] T. H. Stix. *Waves in Plasmas*. American Institute of Physics, New York, 1992.

[16] M. Brambilla. Electron Landau damping of ion Bernstein waves in tokamak plasmas. *Nucl. Fusion*, 38(12):1805, 1998.

[17] M. Brambilla. Numerical simulation of ion cyclotron waves in tokamak plasmas. *Plas. Phys. Control. Fusion*, 41(1):1, 1999.

[18] M. Porkolab, P.T. Bonoli, L. Lin, Y. Lin, E. Nelson-Melby, A. Parisot, J.E. Rice, G. Schilling, J.C. Wright, and S.J. Wukitch. Mode conversion, current drive and flow drive with high power ICRF waves in Alcator C-Mod: Experimental measurements and modeling. In *Proc. 20th IAEA Fusion Energy Conference (Vilamoura, Portugal)*, pages EX/P4–32, 2004.

[19] I. H. Hutchinson, R. Boivin, F. Bombarda, et al. First results from Alcator-C-Mod. *Phys. Plasmas*, 1(5):1511, 1994.

[20] S. J. Wukitch, R. L. Boivin, P. T. Bonoli, J. A. Goetz, J. Irby, I. Hutchinson, Y. Lin, A. Parisot, M. Porkolab, E. Marmar, G. Schilling, and J. R. Wilson. Investigation of performance limiting phenomena in a variable phase ICRF antenna in Alcator C-Mod. *Plas. Phys. Control. Fusion*, 46(9):1479, 2004.

[21] T. E. Tutt. H_α/D_α spectroscopy on Alcator C-Mod. Master's thesis, Massachusetts Institute

of Technology, 1999.

[22] J. W. Heard, C. Watts, R. F. Gandy, and P. E. Phillips. High resolution electron cyclotron emission temperature profile and fluctuation diagnostic for Alcator C-Mod. *Rev. Sci. Instrum.*, 70(1):1011, 1999.

[23] A. Mazurenko. *Phase Contrast Imaging on the Alcator C-Mod Tokamak*. PhD thesis, Massachusetts Institute of Technology, 2001.

[24] H. Weisen. The phase contrast method as an imaging diagnostic for plasma density fluctuations (invited). *Rev. Sci. Instrum.*, 59(8):1544, 1988.

[25] S. Coda and M. Porkolab. Edge fluctuation measurements by phase contrast imaging on DIII-D. *Rev. Sci. Instrum.*, 66(1):454, January 1995.

[26] D. N. Smithe, C. K. Phillips, J. C. Hosea, R. P. Majeski, and J. R. Wilson. Investigation of RF absorption by fast ions and high temperature plasmas using the METS95 wave analysis tool. In *12th Topical Conference on Radio Frequency Power in Plasmas*, volume 403 of *AIP Conference Proceedings*, page 367, New York, 1997. American Institute of Physics.

[27] L. Lao, H. St. John, R. D. Stambaugh, et al. Reconstruction of current profile parameters and plasma shapes in tokamaks. *Nuclear Fusion*, 25(11):1611, November 1985.

[28] E. Nelson-Melby. *Observations and Theory of Mode-Converted Ion Bernstein Waves in the Alcator C-Mod Tokamak*. PhD thesis, Massachusetts Institute of Technology, 2001.

[29] L. Lin, M. Porkolab, D. R. Ernst, et al. Search for TEM and ETG modes with the upgraded PCI diagnostic in Alcator C-Mod. *Bull. American Phys. Society*, 49(8):73, 2004.